

METALLOENZYMES

Conformational dynamics of a multienzyme complex in anaerobic carbon fixation

Max Dongsheng Yin^{1†}, Olivier N. Lemaire^{2†}, José Guadalupe Rosas Jiménez^{3,4}, Mélissa Belhamri², Anna Shevchenko⁵, Gerhard Hummer^{3*}, Tristan Wagner^{2,6*}, Bonnie J. Murphy^{1*}

In the ancient microbial Wood-Ljungdahl pathway, carbon dioxide (CO₂) is fixed in a multistep process that ends with acetyl-coenzyme A (acetyl-CoA) synthesis at the bifunctional carbon monoxide dehydrogenase/acetyl-CoA synthase complex (CODH/ACS). In this work, we present structural snapshots of the CODH/ACS from the gas-converting acetogen *Clostridium autoethanogenum*, characterizing the molecular choreography of the overall reaction, including electron transfer to the CODH for CO₂ reduction, methyl transfer from the corrinoid iron-sulfur protein (CoFeSP) partner to the ACS active site, and acetyl-CoA production. Unlike CODH, the multidomain ACS undergoes large conformational changes to form an internal connection to the CODH active site, accommodate the CoFeSP for methyl transfer, and protect the reaction intermediates. Altogether, the structures allow us to draw a detailed reaction mechanism of this enzyme, which is crucial for CO₂ fixation in anaerobic organisms.

The most ancient pathway for carbon dioxide (CO₂) fixation, the Wood-Ljungdahl pathway, also known as the reductive acetyl-coenzyme A (acetyl-CoA) pathway, is also the most efficient natural CO₂ fixation pathway in terms of adenosine triphosphate (ATP) input (1, 2). This strictly anaerobic process, performed by a wide range of acetogenic bacteria and methanogenic archaea (3), is also used in biotechnology (4–6). In this pathway, the methyl branch transforms CO₂ into a methyl group bound to a cobalamin derivative (hereafter simplified as B12), and the carbonyl branch reduces CO₂ to carbon monoxide (CO). The latter reaction is catalyzed by an Fe-[Ni-3Fe-4S] cluster (C-cluster) in the carbon monoxide dehydrogenase subunit of the bifunctional carbon monoxide dehydrogenase/acetyl-CoA synthase complex (CODH/ACS) (7–17). The branches converge at the Ni-Ni-[4Fe-4S] cluster (A-cluster) localized in the ACS subunit (fig. S1) to generate acetyl-CoA from CO, the methyl group, and CoA (8, 9, 18). Subsequently, acetyl-CoA can be converted to acetate for energy conservation or assimilated into cellular carbon (19, 20). Other microbes use the same enzyme for the reverse process of acetyl-CoA decarbonylation (11, 21, 22).

Structural insights into the catalytic reactions of CODH and ACS have been obtained from

standalone enzymes and bifunctional CODH/ACS complexes, including those from *Moorella thermoacetica*, *Carboxydothermus hydrogiformans*, and *Clostridium autoethanogenum* (Mt, Ch, and Ca, respectively) (8, 9, 12, 15–18, 23, 24). However, the overall molecular mechanism of acetyl-CoA synthesis is still not fully understood owing to the complexity of the reaction, which requires several additional actors and substantial structural rearrangements of the ACS.

In one of the accepted scenarios, the reaction begins with CO₂ reduction at the C-cluster, which requires electron transfer from a ferredoxin (25). The electrons are first transferred to a solvent-exposed [4Fe-4S] cluster (D-cluster, alternatively a [2Fe-2S] cluster) (7, 12, 14, 26–28) located on the symmetry axis of the CODH dimer before being transferred to the C-cluster through an intermediate [4Fe-4S] cluster (B-cluster). Once produced, CO is channeled to the A-cluster through a hydrophobic internal tunneling network and covalently binds as a carbonyl group to the proximal Ni (Ni_p) (8, 16, 23, 29). Subsequently, the methyl-Co(III)-B12, carried by the corrinoid iron-sulfur protein (CoFeSP), interacts with ACS to transfer a methyl cation to the A-cluster (30, 31). The methyl and carbonyl groups react to generate an acetylated A-cluster (32), which promotes the formation of acetyl-CoA through its reaction with the thiol group of CoA.

This reaction mechanism requires flexibility of the ACS as a prerequisite for complete turnover because the ACS must undergo sequential reactions dependent on ferredoxin, gas trafficking, CoFeSP, and CoA. The ACS is composed of three functional domains (A1, A2, and A3, from the N terminus to C terminus) separated by linkers that allow interdomain flexibility. Multiple conformational arrangements of the ACS have been shown through x-ray crystallography and negative-stain electron

microscopy (8, 9, 15–18, 24, 33). However, high-resolution structures of the CODH/ACS complex with its partners or ligands are lacking.

In this study, we aimed to capture the CODH/ACS in action by visualizing the missing conformations in various protein-protein interaction or ligand-bound states. All presented results are derived from proteins anaerobically isolated from the biotechnologically relevant syngas converter *C. autoethanogenum*, an acetogen that we cultivated heterotrophically on fructose in the presence of H₂ and CO₂, as reported previously (16). Previous studies have shown that CODH/ACS from *C. autoethanogenum* catalyzes reversible CO oxidation with artificial electron acceptors or ferredoxin as the physiological partner and methylates the A-cluster with methylcobinamide (16, 34, 35) (see methods). In this work, to structurally characterize the mechanism of acetyl-CoA synthesis, we prepared solutions of CO-treated CODH/ACS-ferredoxin and iodomethane-treated CoFeSP. The solutions were mixed and rapidly plunge-frozen for cryo-electron microscopy (cryo-EM) analysis under anaerobic conditions at ~5% CO in the gas phase. The final mixture contained CODH/ACS heterotetramer, CoFeSP, and ferredoxin in a 1:2:1 molar ratio [all identified by mass spectrometry (16, 34); fig. S2], with iodomethane as the methyl donor and CO as the carbonyl and electron donor. After electron microscopy imaging and initial data processing, we performed three-dimensional (3D) refinement with C₂ symmetry, yielding maps of the rigid core of the enzyme, which is composed of the CODH and A1, at resolutions reaching 1.94 Å (figs. S3 and S4A and tables S1 and S2). By further classifying the CODH/ACS into different states, we gained a detailed view of acetyl-CoA synthesis.

Ferredoxin-dependent CO₂ reduction at the C-cluster

The symmetric map of CODH/ACS exhibited an additional feature, which was not attributable to either the CODH or ACS, at the symmetry axis of CODH. It was further analyzed by focused classification and local refinement without symmetry applied, resulting in a map showing ferredoxin, harboring two [4Fe-4S] clusters, bound asymmetrically near the D-cluster on the C₂ symmetry axis (Fig. 1A and figs. S4B, S5, and S6A). The quality of the density map is substantially lower than that of the rest of the structure, which reflects the expected transient interaction. Hydrogen bonding and hydrophobic contacts stabilize the complex (fig. S6B), forming an interaction network that could be supplemented by electrostatic attraction between positively charged residues (Lys³⁵, Lys⁶³) on the flexible loops of the CODH and the negatively charged area of the ferredoxin (fig. S6C). A previous study questioned the role of the D-cluster as an electron entry or exit point owing to its midpoint potential in

¹Redox and Metalloprotein Research Group, Max Planck Institute of Biophysics, Frankfurt am Main, Germany. ²Max Planck Research Group Microbial Metabolism, Max Planck Institute for Marine Microbiology, Bremen, Germany.

³Department of Theoretical Biophysics, Max Planck Institute of Biophysics, Frankfurt am Main, Germany. ⁴Department of Theoretical Biophysics, IMPRS on Cellular Biophysics, Frankfurt am Main, Germany. ⁵Max Planck Institute of Molecular Cell Biology and Genetics, Dresden, Germany.

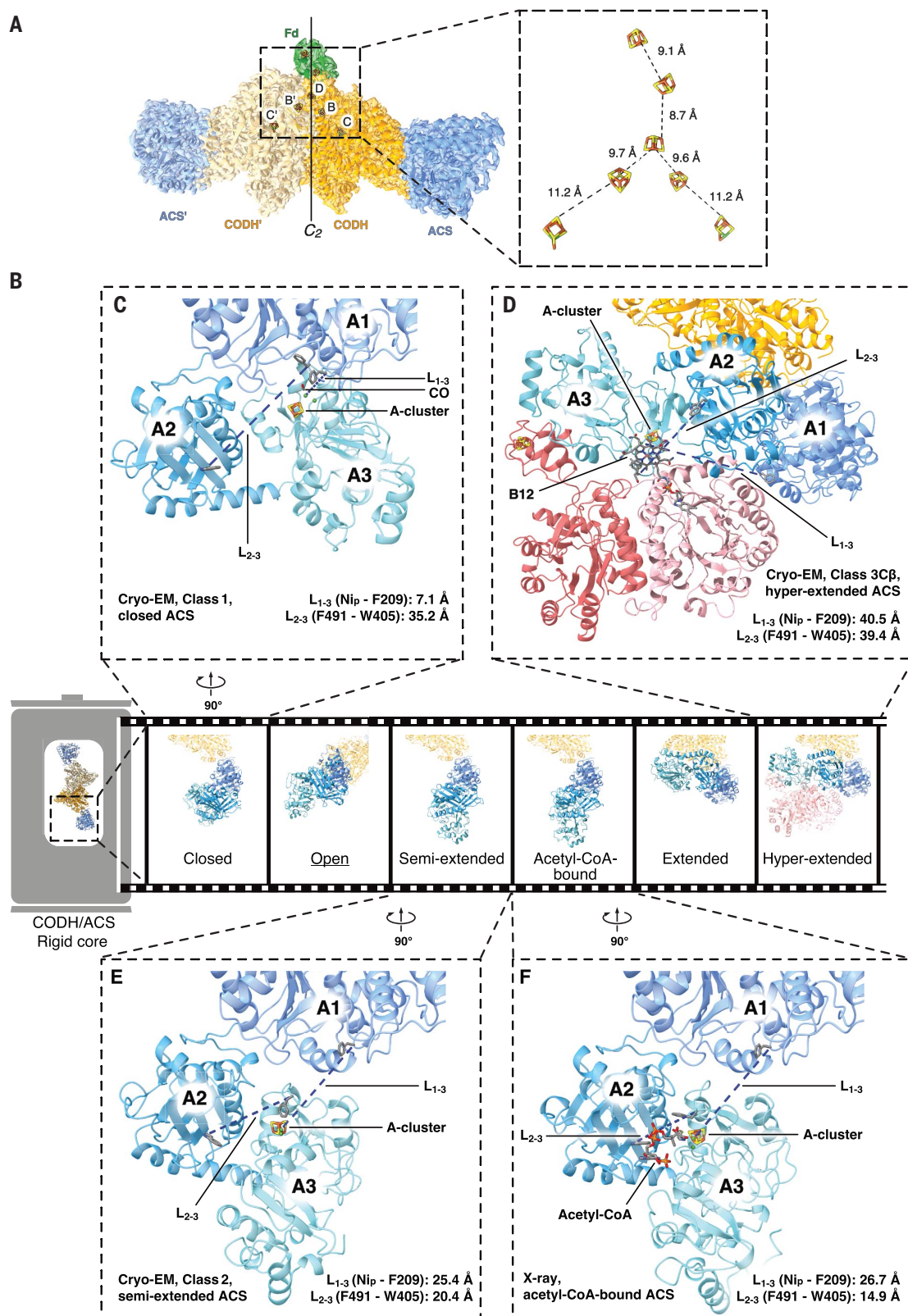
⁶Research Group Microbial Metabolism, Université Grenoble Alpes, CEA, CNRS, IBS, Grenoble, France.

*Corresponding author. Email: bonnie.murphy@biophys.mpg.de (B.J.M.); twagner@mpi-bremen.de (T.W.); gerhard.hummer@biophys.mpg.de (G.H.)

†These authors contributed equally to this work.

Fig. 1. Conformational gallery of the CODH/ACS.

(A) Ferredoxin (Fd, green) docks at the C_2 symmetry axis of CODH (gold and wheat). The symmetry axis is indicated with a vertical line. A1 is displayed in blue. The cryo-EM density of the CODH/ACS-ferredoxin complex is displayed as a surface at 8.8σ , with colors matching the model. As seen in the inset, the binding conformation should allow efficient electron transfer between the [4Fe-4S] cluster of ferredoxin and the D-cluster of CODH; distances are shown as dashed lines. (B to F) The collection of flexible ACS conformations (B), with structures from this study highlighted and aligned based on the A1 domain with the open state obtained from *MtCODH/ACS* (underlined, PDB ID 10AO, chain D) and the extended state (*CaCODH/ACS*, PDB ID 6YTT, chain A) of ACS. The N_{ip} -F209 and F491-W405 distances (defined below as L_{1-3} and L_{2-3} , respectively) for the closed (C), hyperextended (D), semiextended (E), and acetyl-CoA-bound (F) ACS conformations are indicated by dashed lines, with the measured values provided alongside the structures. The ACS domains are shown in shades of blue, from darker at the N terminus to lighter at the C terminus, and the CoFeSP is shown in pink, with a darker shade for its large subunit. All metal cofactors are shown in stick representation. For clarity, the B12 domain of CoFeSP is omitted in (D).



the monofunctional CODH of *Rhodospirillum rubrum* (25, 36). However, the observed interaction and the intercluster distance of 8.7 Å in our structure supports ferredoxin

docking and electron transfer at the D-cluster (Fig. 1A) (7, 12, 26–28, 37). Electrons are then transferred via the B-cluster to the catalytic C-cluster.

The experimental map at the C-cluster shows no evidence of a bound small-molecule ligand (fig. S7). An unrestrained model of the C-cluster exhibited a short distance (2.3 Å) between Ni

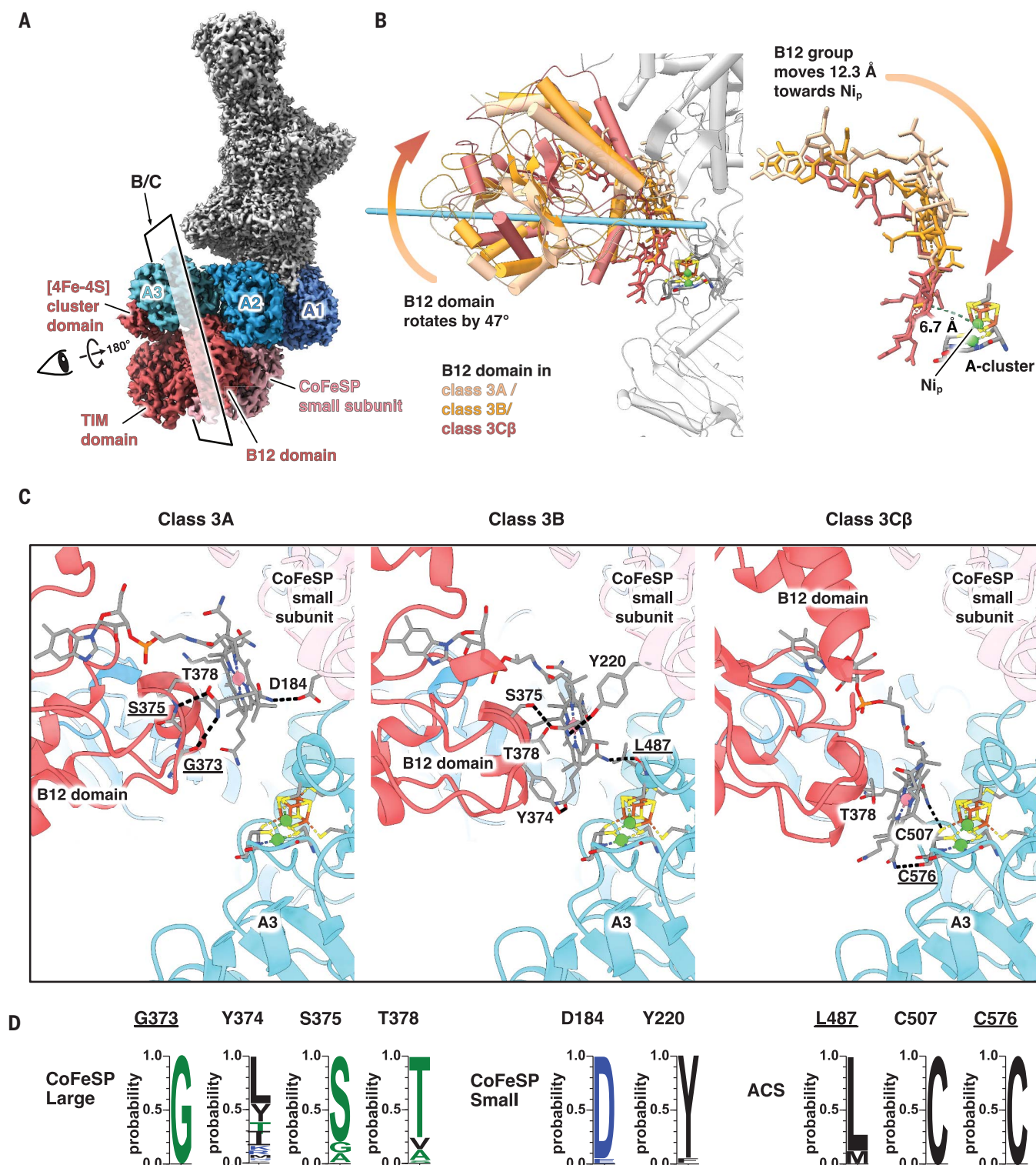


Fig. 2. In the hyperextended, CoFeSP-bound state, rotation of the CoFeSP B12 domain brings the B12 toward the Ni_p. (A) The cryo-EM map of the complex (class 3C β) showing ACS bound to CoFeSP in color, with the rest of the complex in gray. (B) The B12 domain undergoes a 47° rotation (the rotation axis is shown as a light blue bar) from class 3A to class 3C β , positioning the Co atom of B12 6.7 Å away from the Ni_p. The B12 domain and B12 are colored according to the rotational states, as indicated by the color code, and the rest of the complex is gray. (C) Detailed views of the three rotational states, with key hydrogen bonds indicated by dashed lines. Cofactors and residues of interest are

in stick representation. In (A) and (C), the ACS domains are shown in shades of blue, from darker at the N terminus to lighter at the C terminus, and the CoFeSP is colored pink, with a darker shade for its large subunit. (D) Sequence conservation analysis shows that most of the B12-stabilizing residues are well conserved in bacteria and archaea. In both (C) and (D), residues involved in hydrogen bonding through their main chain atoms are underlined. Single-letter abbreviations for the amino acid residues depicted in the figures are as follows: A, Ala; C, Cys; D, Asp; E, Glu; F, Phe; G, Gly; H, His; I, Ile; K, Lys; L, Leu; M, Met; N, Asn; P, Pro; Q, Gln; R, Arg; S, Ser; T, Thr; V, Val; W, Trp; and Y, Tyr.

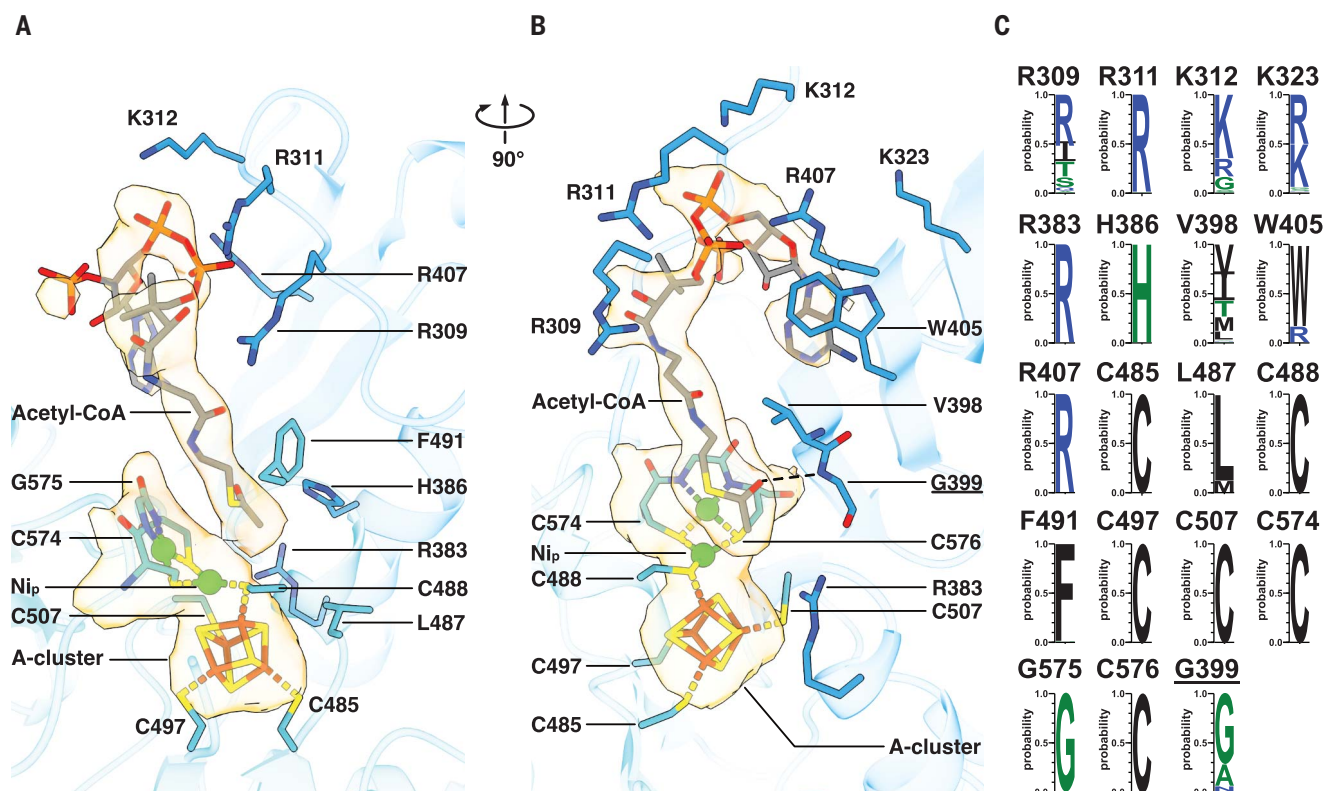


Fig. 3. Crystal structure of the CODH/ACS in the acetyl-CoA-bound state.

(A and B) Close-up views of acetyl-CoA binding, highlighting key interacting residues. The electron density maps ($2F_o - F_c$) for the acetyl-CoA and the A-cluster are shown as light orange surfaces contoured at 1.1σ . A hydrogen bond is indicated by a dashed line. The crystal structure was obtained from a sample different from that used in the cryo-EM analysis. For clarity, residues 323, 398, 399, and 405 in (A) and residues 386, 487, and 491 in

(B) are omitted. ACS is colored light blue; acetyl-CoA and selected residues are shown in stick representation and are colored as follows, except for acetyl-CoA carbon, which is gray: carbon in light blue, oxygen in red, nitrogen in dark blue, sulfur in yellow, phosphorus in light orange, iron in orange, and nickel in green. (C) Conservation of the residues in bacteria and archaea. Residues involved in hydrogen bonding through their main chain atoms are underlined.

and the pendant iron (Fe_u), both refined with partial occupancy (~ 50 and ~ 60 to 70% , respectively). The possibility of a Ni-Fe bond acting as an electron store was previously proposed (38), though the length of a typical Ni-Fe single bond is expected to be on the order of 2.5 \AA (39, 40). Mixed quantum mechanics/molecular mechanics (QM/MM) calculations using density functional theory (DFT) for the quantum region (supplementary text, figs. S8 and S9, and table S3) support this hypothesis, yielding an average Ni- Fe_u distance of 2.5 \AA , which we have modeled accordingly in the C-cluster (fig. S7A).

Conformational spectrum of ACS allows A-cluster carbonylation

Poorly resolved density was present at the expected positions of domains A2 and A3. Using focused classification and refinement of symmetry-expanded datasets (fig. S10), we were able to separate two classes (named class 1 and 2 in the processing workflow, refined to resolutions of 2.83 and 3.29 \AA , respectively) with clear density for A2 and A3 but without additional density attributed to CoFeSP (figs. S4, C and D, S10,

and S11; and tables S2 and S4). The rearrangement of the domains can be modeled as multi-body motion (33) with very low root mean square deviation of each domain across different conformational states and organisms (table S5). Multiple terms have been used to describe the ACS conformation in previous works, such as “open,” “closed,” and “extended.” In this work, we introduce a reference framework for a simple comparison of these states in terms of distances between conserved sites in the three domains. In addition to the global opening and closing of the ACS owing to a highly flexible loop connecting A1 to A2 [previously shown to be highly sensitive to limited proteolysis (16)], the relative positions of A2 and A3 can also undergo an opening-closing movement, allowing or occluding access to the Ni_p independently of the A1 position. To best characterize this dual flexibility, we propose the distances Ni_p -F209 and F491-W405 (*CaACS* numbering, where F is Phe and W is Trp) as proxies of interdomain 1-3 and interdomain 2-3 spacing, respectively (L_{1-3} and L_{2-3} , where L stands for length).

The *CaACS* class 1 resembles the closed conformation of *MtCODH/ACS* and *ChCODH/ACS*

(8, 9, 15, 17), featuring a short L_{1-3} and a long L_{2-3} (Fig. 1, B and C; figs. S12A and S13; and table S6). In the closed state, the A2-A3 space is opened and the A-cluster apposes the A1 surface. A predicted CO channel emanating from the C-cluster opens into a solvent-occluded space around the A-cluster (29). In this state, an additional density observed on Ni_p is modeled as a CO bound to the tetrahedral Ni (fig. S14, A and B). Conserved hydrophobic residues Val¹²⁵, Phe²⁰⁹, and Phe⁴⁹¹ are positioned similarly to their counterparts in the CO-bound state of *MtCODH/ACS* (15) (fig. S14, B and C). These residues were proposed to stabilize the tetrahedral geometry of the carbonylated Ni_p , facilitate CO diffusion through internal cavities to the A-cluster, and hinder the A-cluster from adopting a methylation-compatible geometry (15).

In contrast, class 2 corresponds to the semi-extended state previously described in the crystallographic structure of *CaCODH/ACS* [Protein Data Bank (PDB) ID 6YTT, chain D] (16) (Fig. 1, B and E, and fig. S12B). In this state, A3 is disengaged from A1 and the Ni_p is occluded by the closing of A2-A3 (fig. S13A). The resolution is too limited to describe a bound ligand on the A-cluster

(carbonyl or methyl). Class 2 likely reflects a conformation en route toward CoFeSP docking, in which the Ni_p is protected to avoid side reactions while the interdomain A1-A3 space is gradually opened (table S6).

CoFeSP interaction promotes the ACS hyperextended state

Focused classification of the flexible ACS unveiled a third class corresponding to the CODH/ACS-CoFeSP complex (Fig. 1, B and D; figs. S10,

S11, and S15; and tables S2 and S4). Compared with the extended state obtained by crystallography (PDB ID 6YTT, chain A) (16), ACS complexed with CoFeSP maintains a long L_{1-3} and additionally opens L_{2-3} by means of a 59°

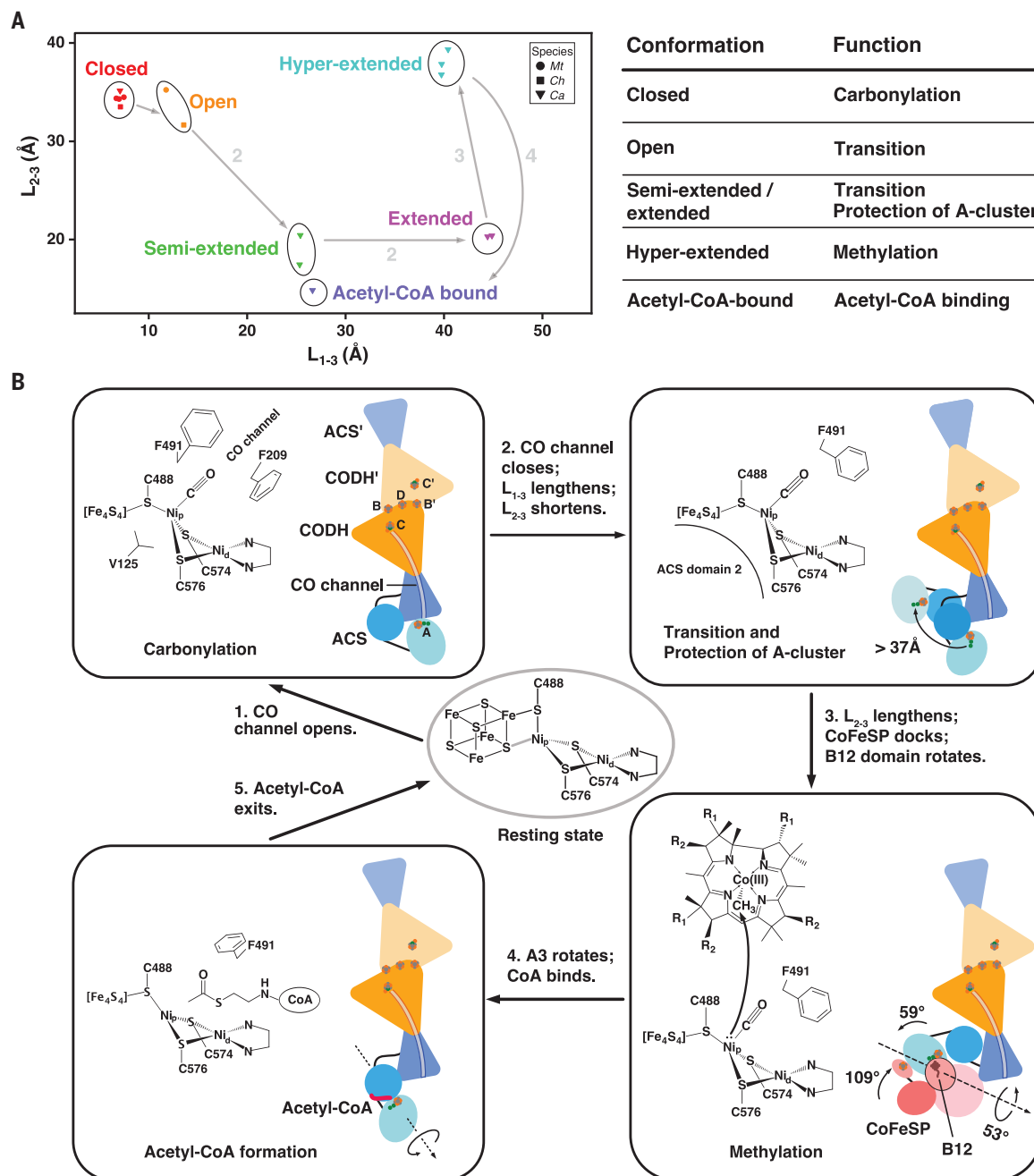


Fig. 4. A conformation-based model of acetyl-CoA synthesis. (A) The conformational 2D spectrum of representative structures of CODH/ACS and monomeric ACS. The L_{1-3} and L_{2-3} distances represent the separations between Ni_p and F209, and between F491 and W405 (CaACS numbering), respectively, and all measured distances are listed in table S6. One proposed reaction route, starting with carbonylation, is marked by arrows and numbered according to the model in (B). The function of each conformation is summarized in the table. (B) A proposed mechanism of acetyl-CoA synthesis in the sequential carbonylation-methylation

scenario. Schematic representation of key CODH/ACS conformations with their functional roles, as well as the corresponding configurations of the A-cluster, are presented in the boxes. The reaction route is labeled with solid arrows, and critical domain motions during the reaction are marked by curved arrows and are further illustrated in figs. S16B, S19A, S28A, and S30. In the ligand-free resting state, the feasible Ni_p -S coordination is indicated by a gray stick. For clarity, the nucleotide tail of B12 is omitted. R_1 denotes the acetamide arm, and R_2 denotes the propionamide arm of the B12 corrin ring.

rotation of A3, leading to a hyperextended state (figs. S13C and S16 and table S6). Consequently, this is the sole state obtained in our study in which the A-cluster is fully accessible for methyl transfer.

The hyperextended state is stabilized by interactions with CoFeSP at three sites: The CoFeSP small subunit docks to both A1 and A3, the [4Fe-4S] cluster domain of the CoFeSP large subunit (residues 1 to 57) interacts with A3 (figs. S17 and S18), and the B12-binding domain (CoFeSP large subunit, residues 326 to 446) also interacts with A3, as discussed below. The distance between the [4Fe-4S] cluster and the A-cluster (32.3 Å; fig. S18) precludes electron transfer, which agrees with previous studies that indicated no direct involvement of the CoFeSP [4Fe-4S] cluster in ACS methylation (41, 42). Rather, our findings support a function of this domain in stabilizing the hyperextended ACS. A comparison of our results with structures of CoFeSP from different species (*Ch*, *Mt*, *Ca*) in isolation and in interaction with the activator or methyltransferase (MeTr) protein partners showed large conformational changes of the [4Fe-4S] cluster and B12-binding domains associated with CoFeSP binding to its partner proteins (fig. S19) (43–45). Residues involved in the interaction between ACS and CoFeSP are mostly conserved among bacteria and archaea (Fig. 2D and figs. S17 and S18), suggesting a similar mode of action across microbial kingdoms.

Methyl transfer reaction through B12 domain motion

The hyperextended state of the ACS enables the bulky CoFeSP to access the A-cluster (class 3; Figs. 1D and 2), but additional motion of the CoFeSP is required to bring the B12 close enough for methyl transfer (43, 45). By 3D variability analysis (3DVA) of class 3, we resolved a rotational motion of the B12-binding domain (Fig. 2B). Supervised classification using three intermediate reconstructions from 3DVA led to three subsets (3A, 3B, and 3C), with 3A and 3B refined to 2.71 and 2.65 Å, respectively (table S2). The subset 3C appeared as a mixture of two states (fig. S20). By building preliminary models for each configuration and using corresponding volumes, which were generated with the ChimeraX molmap command, for supervised classification of class 3C, we obtained two substates, 3C α and 3C β , refined to 2.78 and 2.88 Å, respectively (table S2). These four states represent points along a conformational spectrum in which the B12 domain rotates, allowing B12 to approach Ni_p (Fig. 2, fig. S21, and movie S1), which is reminiscent of the motion described in the *Mt*CoFeSP complexed with its MeTr (fig. S22) (45). In the 3A-3B-3C β sequential movement, the B12 ring progressively breaks all hydrogen bonds with the CoFeSP and establishes new ones with the ACS, including with cluster-ligating cysteine residues of

the A-cluster (Fig. 2C). This rotation also reduces the solvent exposure of the A-cluster [4Fe-4S] cubane. The conserved hydrogen bond-forming residues stabilize the B12 as it moves toward the A-cluster, with the shortest Co-Ni_p distance of 6.7 Å observed in 3C β (Fig. 2, B to D), which is nearly sufficient for direct methyl transfer. We suppose that a transient state exists with a further shortened distance that is suitable for methyl transfer, as in the CoFeSP-MeTr, but this state appears too rare to be captured by classification or 3DVA. No obvious density for a methyl or carbonyl group could be detected at either the corrinoid or the Ni_p site. We assessed the possibility of ligand loss due to radiation damage at the site by reconstructing only early frames, which corresponded to as little as 3.7 megagray (46), but did not observe notable differences in the density (fig. S23A).

In the structures that exhibited no external ligand at Ni_p, models consistently refined to relatively short (bonding) distances between the Ni_p and S1 sulfide of the [4Fe-4S] cluster (fig. S23B). QM/MM calculations (fig. S8, C and D, and supplementary text) indeed predicted that a strong attractive interaction with the [4Fe-4S] cluster would bring Ni_p into bonding distance (fig. S24 and table S7). Therefore, the Ni_p geometry modeled in our ligand-free cryo-EM structures is chemically reasonable, even though a low occupancy (~45 to 59%) of the Ni_p site, the moderate resolution, and the putatively mixed state may hamper the unambiguous interpretation of the Ni_p geometry and the detection of ligands from the potential map.

The acetyl-CoA complex—a snapshot of the bound reaction product

Carbonyl and methyl groups bound at Ni_p combine to form an acetyl (32), which is subsequently transferred to the thiol group of CoA. Despite our efforts, we could not unambiguously detect additional cryo-EM map density in CODH/ACS treated with CoA or acetyl-CoA. However, by cocrystallizing *Ca*CODH/ACS with acetyl-CoA, we obtained a 2.93-Å x-ray structure of the product-bound complex (CODH/ACS_{AC}; Fig. 1F and table S8). The global conformations resemble those of the as-isolated *Ca*CODH/ACS (16) (fig. S25). However, the previously semiextended ACS now exhibits additional density spanning the A2 surface and reaching A3, modeled as acetyl-CoA, whereas the extended ACS of the other asymmetric unit lacks such density, reflecting the requirement for a specific conformation to allow ligand binding (Fig. 3, A and B, and figs. S26 and S27).

The acetyl-CoA primarily interacts with A2 residues, with the adenine group being stabilized by Trp⁴⁰⁵ through π -stacking, and the diphosphate facing a positively charged patch rich in lysines and arginines (Fig. 3B and fig. S27A). The relatively high b-factors of the aden-

osine diphosphate moiety (fig. S27B) indicate only partial stabilization of the acetyl-CoA in the A2-A3 cleft, whose structure is restrained by the crystalline packing.

Compared with the ligand-free semiextended ACS resolved by cryo-EM, acetyl-CoA-bound ACS exhibits a 15° rotation of A3 (fig. S28A), whereas superposition with the previously obtained ligand-free crystal structure shows a more limited rotation of A3 by around 5° (fig. S29), indicating that both crystal packing and ligand binding are likely contributing to the rotation of A3. The rotation allows for additional contacts (Fig. 3), prevents potential clashes (fig. S26B) between acetyl-CoA and A3, and brings the A-cluster into closer proximity to the acetyl-CoA (fig. S28B). In this state, the acetyl-bearing sulfur atom is 4.13 Å away from the Ni_p, and the acetyl group is stabilized by a hydrogen bond between its carbonyl moiety and the main chain of Gly³⁹⁹, as well as an interaction between its methyl moiety and His³⁸⁶ (Fig. 3, A and B). The flexible Phe⁴⁰¹ swings away from the Ni_p (fig. S28C) to provide space for CoA attack. The conserved Arg³⁸³ and His³⁸⁶, located near the A-cluster in the structure (Fig. 3, A and B), are likely crucial for acetyl transfer. Superposition with an acetylated A-cluster structure from a previous DFT study (31) indicates that Arg³⁸³ would be in the direct vicinity of the Ni_p-bound acetyl group, putatively stabilizing it through hydrogen bonding (fig. S28D). His³⁸⁶ is well positioned in our structure to facilitate deprotonation of the thiol group (Fig. 3A), consistent with a previous analysis (18). The majority of the residues involved in acetyl-CoA stabilization in the CODH/ACS_{AC} were already suggested in *Mt*ACS (18), and most of these interacting residues are conserved among bacteria and archaea (Fig. 3C).

Discussion

In this work, we describe structural snapshots of the reaction catalyzed by CODH/ACS upon incubation with ferredoxin, CO, CoFeSP, and iodomethane. We observed a mixture of different states of the complex, which we attribute to the fact that the sample was not under turnover owing to the absence of CoA and to the transient nature of protein-protein interactions.

By providing structural insights into the electron transfer, methyl transfer, and acetyl-CoA formation steps, our work advances decades of studies on the intricate catalytic cycle of the CODH/ACS. The mechanism requires a wide conformational range of ACS mediated by interdomain flexibility, as proposed by previous studies (25, 33). To simplify the nomenclature and comparison of these conformations, we introduced simple metrics based on the interdomain distances L₁₋₃ and L₂₋₃ to allow conformational states to be clustered in a 2D landscape (Fig. 4A and table S6) and to

visualize a conformation-based model of the overall reaction of the CODH/ACS (Fig. 4B). In a sequential carbonylation-methylation scenario, the reaction begins with ferredoxin docking on the D-cluster and the subsequent electron transfer to drive the formation of CO. A closed state of ACS is required to allow the controlled diffusion of CO from the C-cluster to the A-cluster for Ni_p carbonylation (15). To reach the methylation-compatible hyperextended state, the A-cluster-carrying A3 must undock from the A1 and move by around 37 \AA (fig. S30), which could leave the reactive carbonyl- Ni_p site exposed to solvent. This appears to be mitigated by the closing of L_{2-3} in the semi-extended and extended states (Fig. 4A and fig. S13, A and B), which shelters the A-cluster. Upon binding of CoFeSP, the hyperextended state is stabilized, characterized by its long-distance L_{2-3} and exposed A-cluster (Figs. 1D and 4A, fig. S13C, and table S6). The B12 domain of CoFeSP “waltzes” toward this open space, positioning the B12 close enough for the methyl transfer. The carbonyl and methyl groups react to a Ni_p -bound acetyl group, and CoFeSP dissociates from ACS, allowing further conformational change. Although CoA primarily interacts with A2, it must be brought near the A-cluster on A3 to further stabilize the binding and initiate acetyl transfer. Thus, acetyl-CoA formation appears to require a return to shorter L_{2-3} , where A3 is rotated relative to the semiextended state to finely tune the cleft between A2 and A3 for the nucleophilic attack of the thiol group of CoA (fig. S28A). CoA binding may partially drive the A3 rotation, which could explain why this conformation was not observed in our CoA-free cryo-EM sample. After acetyl-CoA release, the ACS returns to the closed conformation for another catalytic cycle.

The proposed scenario does not exclude a reverse sequential order, that is, a sequential methylation-carbonylation process, or the possibility of a random reaction mechanism. We note that among all characterized CaACS structures obtained by cryo-EM from the same sample, a carbonyl ligand is observed only in the closed state, although this may also reflect experimental limitations.

The overall architecture of CaCODH/ACS differs from the model MtCODH/ACS or ChCODH/ACS (16). However, aligning all reported CaACS conformations to the rigid A1 (N-terminal domain) of MtACS does not result in any clashes with the rigid core of MtCODH. This suggests that the conformational states and reaction mechanism described here could be generalized to complexes that include MtCODH/ACS and ChCODH/ACS, in which the N-terminal domain of ACS forms different contacts with the CODH dimer (fig. S31).

To complete the reaction landscape of ACS, several intermediate structures are still needed, including methyl-bound, CO- and methyl-

bound, acetyl-bound, and CoA-bound ACS. Moreover, it will be important to clarify how large-scale conformational changes are triggered or regulated, and how these motions relate to atomic-scale rearrangements at the A-cluster, to understand this reversible and central enzyme in the global carbon cycle.

REFERENCES AND NOTES

- M. C. Weiss *et al.*, *Nat. Microbiol.* **1**, 16116 (2016).
- N. R. Boyle, J. A. Morgan, *Metab. Eng.* **13**, 150–158 (2011).
- O. N. Lemaire, M. Jespersen, T. Wagner, *Front. Microbiol.* **11**, 486 (2020).
- J. K. Heffernan *et al.*, *Front. Bioeng. Biotechnol.* **8**, 204 (2020).
- R. de Souza Pinto Lemgruber *et al.*, *Metab. Eng.* **53**, 14–23 (2019).
- B. Bourgade, C. M. Humphreys, J. Millard, N. P. Minton, M. A. Islam, *ACS Synth. Biol.* **11**, 1790–1800 (2022).
- C. L. Drennan, J. Heo, M. D. Sintchak, E. Schreier, P. W. Ludden, *Proc. Natl. Acad. Sci. U.S.A.* **98**, 11973–11978 (2001).
- T. I. Doukov, T. M. Iverson, J. Seravalli, S. W. Ragsdale, C. L. Drennan, *Science* **298**, 567–572 (2002).
- C. Darnault *et al.*, *Nat. Struct. Biol.* **10**, 271–279 (2003).
- J. H. Jeoung, H. Dobbek, *Science* **318**, 1461–1464 (2007).
- W. Gong *et al.*, *Proc. Natl. Acad. Sci. U.S.A.* **105**, 9558–9563 (2008).
- Y. Kung, T. I. Doukov, J. Seravalli, S. W. Ragsdale, C. L. Drennan, *Biochemistry* **48**, 7432–7440 (2009).
- L. Domnik *et al.*, *Angew. Chem. Int. Ed.* **56**, 15466–15469 (2017).
- E. C. Wittenborn *et al.*, *eLife* **7**, e39451 (2018).
- S. E. Cohen *et al.*, *ACS Catal.* **10**, 9741–9746 (2020).
- O. N. Lemaire, T. Wagner, *Biochim. Biophys. Acta Bioenerg.* **1862**, 148330 (2021).
- J. Ruickoldt, Y. Basak, L. Domnik, J. H. Jeoung, H. Dobbek, *ACS Catal.* **12**, 13131–13142 (2022).
- A. Volbeda, C. Darnault, X. Tan, P. A. Lindahl, J. C. Fontecilla-Camps, *Biochemistry* **48**, 7916–7926 (2009).
- K. Schuchmann, V. Müller, *Nat. Rev. Microbiol.* **12**, 809–821 (2014).
- J. Mock *et al.*, *J. Bacteriol.* **197**, 2965–2980 (2015).
- A. Biester, A. N. Marciano-Delgado, C. L. Drennan, *Biochemistry* **61**, 2797–2805 (2022).
- A. Biester, D. A. Grahame, C. L. Drennan, *Proc. Natl. Acad. Sci. U.S.A.* **121**, e2410995121 (2024).
- T. I. Doukov, L. C. Blasiak, J. Seravalli, S. W. Ragsdale, C. L. Drennan, *Biochemistry* **47**, 3474–3483 (2008).
- V. Svetlichnyi *et al.*, *Proc. Natl. Acad. Sci. U.S.A.* **101**, 446–451 (2004).
- M. Can, F. A. Armstrong, S. W. Ragsdale, *Chem. Rev.* **114**, 4149–4174 (2014).
- H. Dobbek, V. Svetlichnyi, L. Gremer, R. Huber, O. Meyer, *Science* **293**, 1281–1285 (2001).
- J. Chen *et al.*, *Biochemistry* **42**, 14822–14830 (2003).
- E. C. Wittenborn *et al.*, *ACS Catal.* **10**, 7328–7335 (2020).
- A. Biester, S. Dementin, C. L. Drennan, *J. Inorg. Biochem.* **230**, 111774 (2022).
- W. P. Lu, S. R. Harder, S. W. Ragsdale, *J. Biol. Chem.* **265**, 3124–3133 (1990).
- M. Can *et al.*, *J. Am. Chem. Soc.* **145**, 13696–13708 (2023).
- S. W. Ragsdale, H. G. Wood, *J. Biol. Chem.* **260**, 3970–3977 (1985).
- S. E. Cohen *et al.*, *Structure* **29**, 43–49.e3 (2021).
- O. N. Lemaire, M. Belhamri, A. Shevchenko, T. Wagner, *bioRxiv* 2024.07.29.605569 [Preprint] (2024); <https://doi.org/10.1101/2024.07.29.605569>.
- S. Wiley *et al.*, *J. Biol. Chem.* **300**, 107503 (2024).
- J. L. Craft, P. W. Ludden, T. C. Brunold, *Biochemistry* **41**, 1681–1688 (2002).
- C. C. Page, C. C. Moser, X. Chen, P. L. Dutton, *Nature* **402**, 47–52 (1999).
- P. A. Lindahl, *J. Inorg. Biochem.* **106**, 172–178 (2012).
- E. Garcin *et al.*, *Structure* **7**, 557–566 (1999).
- H. Ogata, K. Nishikawa, W. Lubitz, *Nature* **520**, 571–574 (2015).

- S. Menon, S. W. Ragsdale, *Biochemistry* **37**, 5689–5698 (1998).
- S. Menon, S. W. Ragsdale, *J. Biol. Chem.* **274**, 11513–11518 (1999).
- S. Goetzl, J. H. Jeoung, S. E. Hennig, H. Dobbek, *J. Mol. Biol.* **411**, 96–109 (2011).
- S. E. Hennig *et al.*, *Nat. Commun.* **5**, 4626 (2014).
- Y. Kung *et al.*, *Nature* **484**, 265–269 (2012).
- L. A. Baker, J. L. Rubinstein, *Methods Enzymol.* **481**, 371–388 (2010).
- J. G. Rosas-Jimenez *et al.*, QM/MM calculations and geometry optimizations of C- and A-clusters in CODH/ACS, the key enzyme in the Wood-Ljungdahl pathway. Version v1. Zenodo (2024); <https://doi.org/10.5281/zenodo.12705281>.
- O. N. Lemaire, Sequence alignments for the determination of residue conservation in ACS, CoFeSP large subunit and CoFeSP small subunit. Version v1. Zenodo (2024); <https://doi.org/10.5281/zenodo.12785604>.
- A. Shevchenko, MS raw data for “Conformational dynamics of a multienzyme complex in anaerobic carbon fixation.” Version v1. Edmond (2024); <https://doi.org/10.17617/3.02LZW1>.

ACKNOWLEDGMENTS

The Redox and Metalloprotein research group is grateful to the Central Electron Microscopy Facility at the Max Planck Institute of Biophysics for providing cryo-EM infrastructure and technical support and to the Max Planck Society for their support. We thank R. Zimmermann for her expertise and support in the anaerobic work. The Microbial Metabolism research group thanks the Max Planck Institute for Marine Microbiology and the Max Planck Society for their continuous support. We also thank C. Probian and R. Appel for their assistance in the Microbial Metabolism laboratory. We thank the Swiss Light Source (SLS) synchrotron, especially the staff of beamline X06DA. **Funding:** This work was supported by funding from the Max Planck Society (to B.J.M., T.W., and G.H.) and the German Research Foundation (Heinz Maier-Leibnitz prize funding to B.J.M.). T.W. was additionally supported by the Deutsche Forschungsgemeinschaft priority program 1927, “Iron-Sulfur for Life” WA 4053/1-1. **Author contributions:** Conceptualization: B.J.M., T.W., M.D.Y., O.N.L.; Methodology: M.D.Y., O.N.L., J.G.R.J., A.S., G.H., T.W., B.J.M., M.B.; Investigation: M.D.Y., O.N.L., J.G.R.J., M.B., A.S.; Visualization: M.D.Y., O.N.L., J.G.R.J., A.S.; Funding acquisition: B.J.M., T.W., G.H.; Project administration: B.J.M., T.W., G.H.; Supervision: B.J.M., T.W., G.H.; Writing – original draft: M.D.Y., O.N.L., J.G.R.J., B.J.M., T.W.; Writing – review and editing: M.D.Y., O.N.L., J.G.R.J., M.B., A.S., G.H., T.W., B.J.M. **Competing interests:** The authors declare no competing interests. **Data and materials availability:** Cryo-EM structures of the CODH/ACS are available from the PDB under accession codes 9FZY (CoFeSP-bound state, class 3A), 9FZZ (CoFeSP-bound state, class 3B), 9G00 (CoFeSP-bound state, class 3C), 9G01 (closed and CO-bound state), 9G02 (semiextended state), and 9G03 (ferredoxin-bound state). Maps and half-maps are available from the Electron Microscopy Data Bank (EMDB) under accession codes 50897 to 50909. The crystal structure of acetyl-CoA-bound CODH/ACS is available from the PDB under accession code 9G7I. Atomic coordinates from the QM/MM calculations are archived in Zenodo (47). The sequence alignment files used for the construction of figures are also archived in Zenodo (48). Raw mass spectrometry data are archived under accession code 02LZW1 in Edmond (49), an open research 2data repository of the Max Planck Society. **License information:** Copyright © 2025 the authors, some rights reserved; exclusive licensee American Association for the Advancement of Science. No claim to original US government works. <https://www.science.org/about/science-licenses-journal-article-reuse>

SUPPLEMENTARY MATERIALS

science.org/doi/10.1126/science.adr9672
Materials and Methods
Supplementary Text
Figs. S1 to S31
Tables S1 to S8
References (50–87)
MDAR Reproducibility Checklist
Movie S1

Submitted 31 July 2024; accepted 25 November 2024
10.1126/science.adr9672